Surface & Coatings Technology 526 (2026) 133329

Contents lists available at ScienceDirect

Surface & Coatings Technology

journal homepage: www.elsevier.com/locate/surfcoat

Hydrothermal temperature-dependent growth and tribological performance of Mg–Al–Ce LDH/CeO_2 composite coatings on AZ31 Mg alloy

Feng Liu [a], Peitao Guo [a,*], Zhen Li [a], Lu Li [a,*]

[a] Southwest Mountain Regions Intelligent Agricultural Machinery Equipment Innovation Center, School of Materials and Energy, Southwest University, Chongqing, 400715, China

ARTICLE INFO

Keywords:
MgAlCe-LDH/CeO_2 composite coating
CeO_2 nanoparticles
Hydrothermal temperature
Wear-resistant performance

ABSTRACT

A composite coating consisting of magnesium–aluminum–cerium layered double hydroxide and cerium oxide (MgAlCe-LDH/CeO_2) was generated on AZ31 Mg alloy by hydrothermal treatment combined with a rare-earth conversion process. The effect of hydrothermal temperature (120–160 °C) on surface morphology, mechanical performance, and tribological behavior was systematically assessed. At low temperatures, the MgAlCe-LDH and CeO_2 particles showed heterogeneous dispersion, which reduced mechanical performance and increased the wear rate. Increasing the temperature to 160 °C induced local agglomeration and coarsening in the microstructure, producing a pronounced deterioration in overall performance. At the optimal temperature of 150 °C, the coating exhibited a compact architecture comprising uniformly oriented MgAlCe-LDH and homogeneously distributed CeO_2 particles, without visible cracking or porosity. This microstructural integrity produced the optimal mechanical performance, the lowest friction coefficient (0.08), and the minimum wear rate (0.39×10^{-4} $mm^3 \cdot N^{-1} \cdot m^{-1}$), corresponding to a 95% reduction over the AZ31 substrate. The mechanisms underlying the synergistic enhancement of mechanical and tribological behavior were accordingly analyzed. These findings demonstrated that precise regulation of hydrothermal temperature significantly improved the microstructure, mechanical performance, and wear resistance of the MgAlCe-LDH/CeO_2 composite coating, offering a feasible strategy for improving the service life of AZ31 Mg alloy in engineering applications.

1. Introduction

AZ31 magnesium alloy shows broad application prospects in lightweight structure fields such as aerospace, automobile manufacturing, and electronics due to its low density, high specific strength [1–3]. However, the low surface hardness and wear resistance have seriously restricted its large-scale application in lightweight and high wear scenarios such as high-performance transmission pairs [4,5]. Traditional surface modification technologies faced challenges in balancing wear resistance and process practicality. For example, although micro-arc oxidation (MAO) can produce a hard ceramic layer, its high energy consumption and porous structure (microcracks and micropores) often damage the fatigue strength of the substrate and become a penetration channel for corrosive media [6]; while thermal spray coatings often peel off under mechanical stress due to insufficient bonding strength with the substrate [7]. Therefore, the development of an energy-efficient, environmentally friendly coating that not only precisely regulates the microstructure, but also has a synergistic effect of efficient lubrication and wear resistance is critical to expanding the application of AZ31 Mg alloys.

In various surface treatment schemes, MgAl-LDH coatings grown by in-situ hydrothermal method showed advantages of environmental friendliness and low cost in the preparation process [8]. MgAl-LDH is a kind of hydroxide with a two-dimensional layered structure. Its positively charged laminae are composed of Mg—O and Al—O octahedral units, and charge compensation anions such as nitrate or carbonate are accommodated between layers through electrostatic interactions and hydrogen bonding. In the field of tribology, MgAl-LDH was considered to be an ideal solid lubricating and protective material suitable for Mg alloys [9]. Its lubricating mechanism was mainly due to the weak interlayer bonding force between nanolayers, which tended to undergo interlayer peeling and relative sliding under shear load, thus forming a lubricating film with low shear characteristics in the contact area of friction pairs [10,11]. In addition, the nanosheets formed by exfoliation could effectively fill microcracks and rough valleys on the substrate surface, resulting in significant repair and polishing effects [12,13].

* Corresponding authors.
E-mail addresses: shuibianhe218@163.com (P. Guo), lilu.swu@gmail.com (L. Li).

https://doi.org/10.1016/j.surfcoat.2026.133329
Received 17 December 2025; Received in revised form 8 February 2026; Accepted 24 February 2026
Available online 26 February 2026
0257-8972/© 2026 Elsevier B.V. All rights are reserved, including those for text and data mining, AI training, and similar technologies.

However, single-component MgAl-LDH coatings still faced many challenges in engineering applications. Limited by the preparation, the thickness of coatings obtained by conventional processes usually fluctuated in the range of 5 to 20 μm, which was difficult to meet the long-term service requirements under heavy-load conditions [14]. Meanwhile, the microstructure of a single MgAl-LDH coating was relatively loose, and there were obvious micropores and defects, which not only weakened its effectiveness as a physical barrier but also made it prone to collapse under extreme friction stress, resulting in fluctuations of the friction coefficient and inducing severe wear [15]. Therefore, how to improve the mechanical support and compactness is the core problem to be solved in the research field of MgAl-LDH coatings.

Focusing on the optimization of coating properties, researchers have carried out extensive explorations from the aspects of microstructure regulation and component co-design. It was reported that by constructing LDH and MOF composite structures, the thickness of the coating was 9.1 μm after 10 h of reaction [16]. Zhao et al. prepared a modified LDH coating on AZ31 alloy, achieving a thickness of 23.8 μm and a reduced friction coefficient (COF) of ~0.25 (with a wear rate of 0.1) after a 12 h reaction cycle [17]. Additionally, another study prepared MgAl-LDH/Al_2O_3 composite coatings by the hydrothermal method; after 12 h of reaction, the thickness was ~3.66 μm, and the COF was maintained at about 0.28 [18]. The above results showed that the existing multi-step modification or composite strategies generally suffered from long reaction cycles, complicated processes, or low coating thickening efficiency [19]. In addition, many studies depended on mechanically mixing of pre-synthesized nanoparticles into the reaction system, which easily led to particle agglomeration and insufficient interfacial bonding force between particles and the LDH matrix. Under this background, the introduction of cerium (Ce) with good environmental compatibility and significant modification effect was gradually regarded as a promising solution approach [20]. This element could form a dense and uniform conversion layer during the in-situ reaction process. Depending on the reversible redox properties between Ce^{3+} and Ce^{4+}, it could also endow the coating with unique self-healing capabilities and superhydrophobic properties [21,22]. However, at present, research on hydrothermal-treatment fabricated CeO_2/MgAl-LDH composites has only been found in the photocatalytic field, such as the visible light-induced water reduction reaction [23], and research on the tribological properties of this system is very scarce. Moreover, the hydrothermal temperature, as a key parameter regulating nucleation kinetics, crystal growth rate, and Ce^{3+}/Ce^{4+} conversion rate, has not yet been fully revealed.

In this work, MgAlCe-LDH/CeO_2 composite coatings were fabricated on AZ31 Mg alloy via a one-step hydrothermal method. The effect of hydrothermal temperature (120–160 °C) on the formation kinetics, thermodynamics, and the resulting mechanical and tribological properties of the coatings was systematically investigated. Precise adjustment of hydrothermal temperature optimized the redox kinetics of Ce^{3+}/Ce^{4+}, which significantly lowered the nucleation barrier of LDH on the substrate surface and thus enabled the construction of a crack-free, high-density hierarchical composite structure with a simplified process. The experimental results demonstrated that at the optimal temperature of 150 °C, the coating exhibited a synergistic enhancement in mechanical and tribological properties: it showed a significant increase in hardness, a friction coefficient as low as 0.08, and a wear rate reduced by 95% compared with that of the AZ31 substrate. These findings clarified the physicochemical synergistic mechanism of hard CeO_2 particles and two-dimensional LDH lamellae in load-bearing and interfacial lubrication, and provided a generalizable microstructure–property control strategy for the development of high-performance wear-resistant magnesium alloys.

2. Materials and methods

Commercial AZ31 Mg was provided by Dongguan Hongdi Metal Materials Co., Ltd., as the experimental material. Test pieces were cut into 10 mm × 10 mm × 3 mm to be used as the substrate. Each sample was sequentially ground with 600 # to 2000 # silicon carbide (SiC) sandpaper. Then it was washed with alcohol in an ultrasound for 5 min, and finally air-dried for later use. The hydrothermal treatment solution was prepared via combining $Ce(NO_3)_3{\cdot}6H_2O$ with deionized water to get 10 g/L, with a solution pH of 4. The samples were placed in the 20 mL polytetrafluoroethylene reactor liner, and 8 mL of the hydrothermal treatment solution was added to ensure complete submersion of the samples. The reactor containing the liner was placed inside an electric hot air drying oven (101-1BS) and subjected to heating from 120 °C up to 160 °C in jumps of 10 °C increments using a rapid heating-hold mode for 3 h (sample designated HT120-HT160). A control sample (HTDI) was prepared with DI water at 150 °C. As it cooled down to room temperature, samples were freed from the reactor, washed with DI water, and dried. The detailed parameter optimization procedures are provided in Section 1 of the Supplementary Material. Preparation procedures are shown in Fig. 1.

Microstructure examination was conducted using a scanning electron microscope (SEM, JSM-6610) equipped with an electron backscatter diffraction system (EBSD, Oxford Instruments AZtecHKL). After the AZ31 substrate was ground with SiC sandpaper, it was electrolytically polished for about 60 s at a voltage of 20 kV in AC2 solution under liquid nitrogen cooling. The step size was set to 1.2 μm during the EBSD test. The average value of the coating thickness was calculated after five repeated measurements by cross-sectional SEM in accordance with ASTM B748–90 (2021). The calculation of the coating deposition rate is documented in Section 2 of the Supplementary Material. The chemical composition of the composite coating was analyzed by using an energy dispersive spectrometer (EDS). X-Ray Diffraction (XRD-6100, Shimadzu, Japan) was used to characterize the phase structure of the coating. The instrument parameters were set as follows: Cu Kα radiation, tube voltage 40 kV, a 2θ angle ranging from 10° to 80° with a testing rate of 5° min^{-1}. MDI Jade 6 software was used to carry out the phase analysis. The chemical valence states of the coating elements were determined using X-ray photoelectron spectroscopy (XPS) (AXIS SUPRA+, Shimadzu, Japan) with a monochromatic Al Kα radiation source. The measurements were carried out in single-point sampling mode at room temperature and vacuum conditions. Data analysis was performed using Advantage software for peak fitting. Utilizing the C 1s spectral peak at 284.8 eV as the reference for charge adjustment, the data were processed. The spectral peak fitting range was established, and the FWHM was constrained to a rational and uniform range. The relative location and area ratio of each peak were regulated within an acceptable range, exemplified by a Ce $3d_{5/2}$:$3d_{3/2}$ area ratio of 3:2. By quantifying the peak area of distinctive peaks utilizing Origin software, the chemical states were quantified.

The digital micro-hardness tester (HVS-1000A, Lraizhou Huayin) was used to measure the micro-hardness. The loading time was maintained at 10 s. Based on the principle that the depression depth should be less than 10% of the coating thickness, it was determined that the optimal load for the hardness test was 10 gf (Fig. S4). According to ASTM E384–22, each sample was measured six times, and the final result was based on its average value as valid data. Adhesion strength was measured on the multifunctional material surface property tester (MFT-4000, Lanzhou, Huahui, China). In accordance with ASTM C1624–22, a diamond conical tip was chosen, including a 200 μm radius and 120° conical angle, to handle the scratch test within 10 mm. Scratch load built up from 0 to 50 N following a 100 N·min^{-1} pace. The critical failure load was determined by the exposure of the substrate, used to characterize adhesion strength, and three tests were performed to determine its average. The surface roughness was detected by a three-dimensional (3D) profilometer (Superview W1, CHOTEST) in accordance with ASTM E1274–18 (2024), and the mean square root deviation (S_q) as well as the average height difference (S_a) were calculated. Frictional wear testing was conducted using a dynamic damage protection

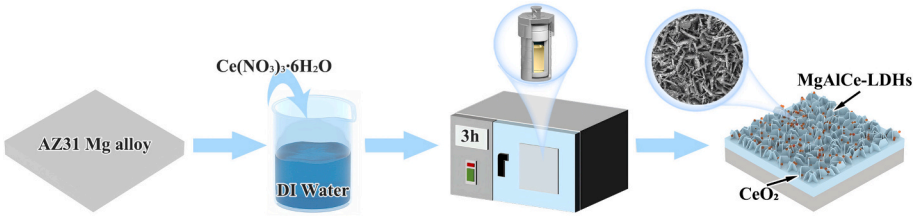

Fig. 1. Schematic illustration of the preparation process of MgAlCe-LDH/CeO_2 composite coating on the AZ31 Mg alloy.

tester (AS5430, Lanzhou, Huahui, China) in accordance with ASTM G133–22. Based on the optimization strategy (Figs. S2 and S3), this study determined that the friction test would be carried out under the following conditions: apply load 10 N, sliding frequency 5 Hz (f), a stroke of 5 mm (l), for a duration of 20 min, in the presence of a Φ6 mm Al_2O_3 ceramic friction ball. To assess long-term durability and ultimate bearing capacity, tests of extended duration (60 min and 120 min) and higher intensity (20 N, 10 Hz) were also performed. All experiments were repeated three times to ensure repeatability. The micromorphology of the wear track was analyzed using SEM, and a 3D profilometer was employed to generate contour maps of the wear profile. Three wear tests were repeated under the same parameters to ensure reproducibility, and the average cross-sectional area (S) of the wear track was calculated by taking the average value of the wear track profile curve in Xtreme Vision software. The sliding distance (L) was calculated using the $L = f \times l \times t$ formula. The wear rate was calculated from the following formula [24]:

$$K = \frac{S \times l}{F \times L} \tag{1}$$

where K is the wear rate ($mm^3 \bullet N^{-1} \bullet m^{-1}$), F represents the load (N), S is the average cross-sectional area (mm^2), L is the sliding distance (m), and l is the length of the wear track (mm).

3. Results

3.1. Substrate microstructure

Fig. 2 displays the microstructure characteristics of the substrate. The grain orientation map (Fig. 2a) showed that the grain size approximately followed a normal distribution, and its average size was 10.65 μm. This indicated that the substrate had fine grains and a narrow size distribution, reflecting good microstructural uniformity. The corresponding (0001) pole figure (PF) further illustrates that the c-axes of the grains are mainly aligned parallel to the normal direction (ND), and the orientations are mainly concentrated in the center of the pole, which is a characteristic of the typical matrix structure of a rolled Mg alloy. The misorientation distribution of the grain boundaries (Fig. 2b) shows that the proportion of high-angle grain boundaries (HAGBs) is 80.7%, and the average orientation angle was 27.6°. This indicated that the microstructure consisted mainly of recrystallized grains, with a stable grain boundary configuration and uniform distribution, thus improving the microstructural uniformity. Beyond that, the distribution of geometrically necessary dislocations (GNDs) as shown in Fig. 2c evidences a fairly restrained overall dislocation density, averaging 3.18 × 10^{13} m^{-2}, suggesting the substrate faces minimal residual stress. Taken together, the fully recrystallized AZ31 Mg substrate manifests qualities such as fine and fairly even grain sizes, broadly uniform grain orientation patterns, and a condition of reduced residual stress. This dependable microstructure acts to reduce the effects of the starting substrate on the ensuing hydrothermal process, hence permitting an equitable analysis of how hydrothermal temperature affects the coating's microstructure and attributes within uniform initial settings.

3.2. Phase identification

3.2.1. XRD analysis

XRD spectra of MgAlCe-LDH/CeO_2 composite coating produced at various hydrothermal reaction temperatures are displayed in Fig. 3. Except for the HT160 sample, all coatings showed the LDH characteristic

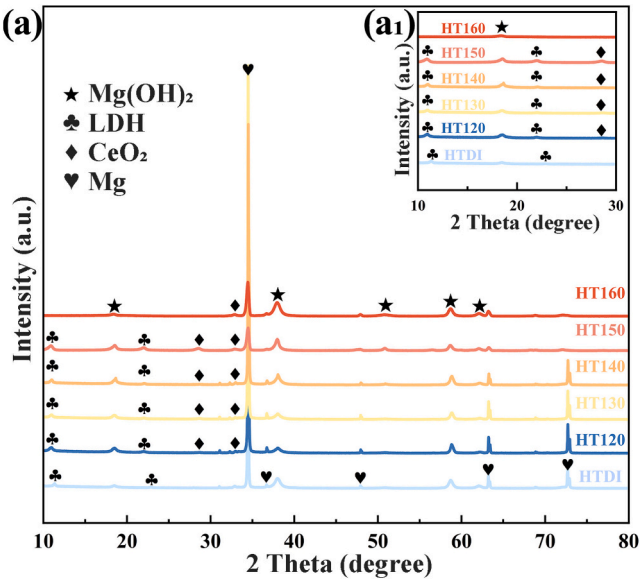

Fig. 3. XRD patterns of the MgAlCe-LDH/CeO_2 composite coating (a); enlarged view of the selected 2θ region from 10° to 30° (a_1).

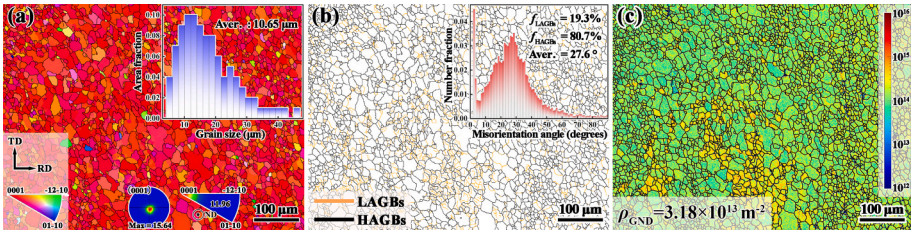

Fig. 2. EBSD analysis of the AZ31 Mg alloy substrate: (a) grain orientation map, (0001) pole figure, and ND inverse pole figure; (b) grain boundary characteristics and misorientation angle distribution; (c) geometrically necessary dislocation map.

diffraction peaks at 2θ angles of 10.95° and 21.9°, corresponding to (003) and (006) crystal planes, respectively [25].

Peaks attributable to $Mg(OH)_2$ showed up at 2θ angles of 18.4°, 37.9°, 50.8°, 58.6°, and 62.2°. For the HT160 sample, only the 33.1° CeO_2 reflection was observed, whereas the HT120 to HT150 samples showed CeO_2 diffraction peaks at both 28.6° and 33.1°. This indicated that elevated hydrothermal temperature accelerated growth kinetics and selectively suppressed the (111) orientation of CeO_2 [26]. As evident in Fig. 3a_1, the intensity of the LDH diffraction peak shows a strong trend with the increase of temperature; however, no appreciable LDH signal can be identified in the HT160 sample. These observations suggested that higher temperatures elevated the crystallization degree of LDH, yet surplus heat induced some degree of amorphization. Also, the diffraction signals for CeO_2 and LDH within the HT150 coating demonstrated enhanced distinctness when set beside counterparts in alternative specimens, stressing that 150 °C afforded the supreme conditions for advancing both constituents. Altogether, the MgAlCe-LDH/CeO_2 composite coating predominantly held CeO_2, $Mg(OH)_2$, and LDH, with the beginning of those aspects displaying plain reliance on the hydrothermal temperature.

3.2.2. XPS analysis

Fig. 4 indicates the XPS spectrum of MgAlCe-LDH/CeO_2 composite coating. The complete scanning spectrum in Fig. 4a showed five characteristic peaks, confirming that these five elements were present in the composite coating. The carbon signal and some of the oxygen signal may come from surface pollutants introduced during air exposure [21]. Two peaks were obtained from the O 1s spectrum (Fig. 4b) through deconvolution analysis: the strong peak at 529.8 eV was attributed to the Ce oxide compounds, while the secondary peak at 531.7 eV was related to the Al-OH group. This indicated that Ce was incorporated into the coating in the form of Ce^{3+}/Ce^{4+} oxides, and that $Al(OH)_3$ was also present. The Mg 2p high-resolution spectrum (Fig. 4c) showed two fitted peaks at 48 eV and 49.4 eV, corresponding to metallic Mg and $Mg(OH)_2$, respectively [27]. In the Al 2p spectrum (Fig. 4d), the characteristic peak at 72.8 eV corresponded to Al^{3+} species.

The Ce 3d spectrum (Fig. 4e) shows three characteristic regions typical of Ce, and the peak deconvolution confirmed that both Ce^{3+} and Ce^{4+} existed. According to the spin-orbit splitting behavior of the Ce 3d orbital, the energy level was divided into two energy bands, a lower and a higher one, namely the $3d_{5/2}$ subshell with lower binding energy and the $3d_{3/2}$ subshell with higher binding energy. Ce^{3+} and Ce^{4+} have their own characteristic peaks in both split states [28]. In the $3d_{5/2}$ region, the peaks at 897.7 eV and 888.1 eV were Ce^{4+}, while the peak at 881.7 eV corresponded to Ce^{3+}. In the $3d_{3/2}$ region, the peaks at 901.5 eV, 915.2 eV, 916.5 eV, and 917.4 eV were attributed to Ce^{4+}, while the peak at 906.7 eV was attributed to Ce^{3+}. Furthermore, Origin software was used to integrate the area of the characteristic peaks, and the atomic sensitivity factor method was used for element quantitative analysis. Relative atomic concentration C_X [29] was calculated by the formula:

$$C_X = \frac{A_X/S_X}{\sum (A_i/S_i)} \quad (2)$$

where X and i represent the calculated and constituent atom, respectively, A is the integral intensity of the photoelectron signal, and S is the relative atomic sensitivity factor.

XPS peak-area analysis indicated that Ce predominantly occurred in the Ce^{4+} valence state, demonstrating that CeO_2 served as the principal Ce-bearing phase. Thus, the XPS spectra confirmed that MgAlCe-LDH/CeO_2 composite coating consisted of CeO_2, $Mg(OH)_2$, and LDH phases, in agreement with the XRD results.

3.3. Microstructure characterization

3.3.1. SEM and EDS analysis

Fig. 5 shows the surface micromorphology characterization of composite coatings prepared at various hydrothermal temperatures. These composite coatings generally exhibited good density, but there were significant differences in their structure and morphological characteristics. As the reaction temperature increased, the number of surface cracks and pores (shown by the arrows in Fig. 5a–c) gradually decreased. The HT150 sample (Fig. 5d) surface was evenly covered with a dense nanosheet structure, and there were no obvious cracks or pores. Zhang et al. [30] previously reported a similar LDH nanosheet morphology, consistent with the characteristic LDH diffraction peaks observed in the corresponding XRD pattern. The HT160 sample formed a locally aggregated nanoblock structure, and some nanosheets were still retained at the bottom layer. The significant coarsening of the surface microstructure masked most of the LDH nanosheets, which explained why there was no obvious LDH diffraction peak in the XRD pattern of the HT160 sample.

To explore the distribution and composition of elements, EDS analysis was performed on HT130 and HT150 under the same conditions. As illustrated in Fig. 5b and d, an elevated hydrothermal temperature significantly promoted the doping and distribution uniformity of Ce elements, indicating that the higher temperature environment was conducive to the formation of Ce-containing compounds. In addition, EDS point analysis of representative areas (Table 1) showed that the nanosheet-like LDH structure (point 1, Fig. 5d) in the HT150 sample was

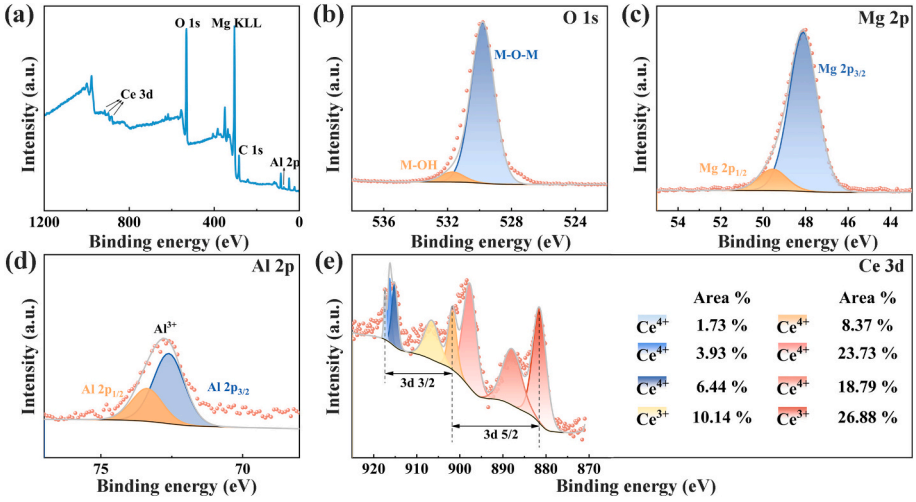

Fig. 4. XPS survey spectrum of the composite coatings (a) and high-resolution spectra of O 1s (b), Mg 2p (c), Al 2p (d), and Ce 3d (e).

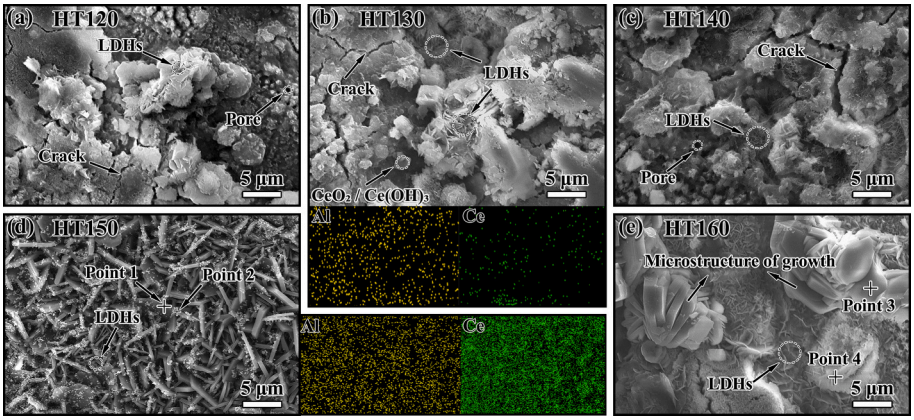

Fig. 5. Surface SEM images of the MgAlCe-LDH/CeO_2 composite coating prepared at hydrothermal temperatures of (a) 120 °C, (b) 130 °C, (c) 140 °C, (d) 150 °C, and (e) 160 °C.

Table 1
The EDS point analysis results (at.%).

Element	Point 1	Point 2	Point 3	Point 4
O	62.27	62.05	64.30	64.40
Mg	36.90	31.63	35.50	27.00
Al	0.00	0.00	0.10	1.90
Zn	0.00	0.00	0.00	0.10
Ce	0.83	6.32	0.00	6.60

rich in Mg and Al but contained little Ce, while the spherical particles attached to the nanosheets (point 2, Fig. 5d) showed a relatively high Ce content. According to previous literature [17], the nanosheet and spherical particles can be identified as $Mg(OH)_2$ and CeO_2 and/or $Ce(OH)_3$. In contrast, no Ce signal was detected in point 3 of the HT150 sample. Based on the XRD spectrum results (Fig. 3), its phase could be determined as $Mg(OH)_2$. However, point 4 showed significant Ce enrichment, and its aggregation morphology and element composition were consistent with CeO_2, which was reported in earlier studies [25].

In summary, increasing the hydrothermal reaction temperature effectively inhibited the generation of surface pores and cracks and promoted the transformation from discrete nanosheet-like LDH to dense structures, which was interspersed with Ce-enriched spherical particles. This structure was finally aggregated and coarsened at 160 °C. Thus, the high-temperature environment not only promoted the growth of the LDH phase but also improved the uniformity of element distribution, demonstrating that the coating formation process is significantly temperature-dependent.

3.3.2. Cross-sectional morphologies of MgAlCe-LDH/CeO_2

Fig. 6 shows the cross-sectional microstructure of MgAlCe-LDH/CeO_2 composite coating prepared at various hydrothermal reaction temperatures. In general, all coatings showed good adhesion to the substrate and relatively dense microstructure, but the thickness showed a clear and significant trend of change. The thickness of the HT150 coating reached its maximum value of 41.49 μm, and its fastest deposition rate was 13.83 μm/h (Table S1), while the HT160 sample decreased significantly to 29.67 μm. This phenomenon may be related to excessive nucleation in a high-temperature environment–high temperature caused some reaction products to precipitate as powder in the solution instead of forming a deposition on the surface, thus limiting the further growth of the coating.

Fig. 6d illustrates the much denser and defect-free microstructure of the HT150 coating. Evidently, the coating was absence of internal microcracking and remained a flawless, intimate adhesion to the substrate. This remarkable structural integrity enhanced the load-bearing capability, resulting in improved tribological performance. Conversely, when the hydrothermal temperature increased, significant cracks emerged within the HT160 covering (Fig. 6e). This was primarily due to stress concentration arising from thermal mismatch during coating deposition and cooling [32], which eventually compromised the structural integrity of the coating and diminished adhesion strength.

3.4. Mechanical and surface characteristics

3.4.1. Coating microhardness

Fig. 7a illustrates the evolution of coating microhardness as a function of hydrothermal temperature. The hardness initially rose, reaching

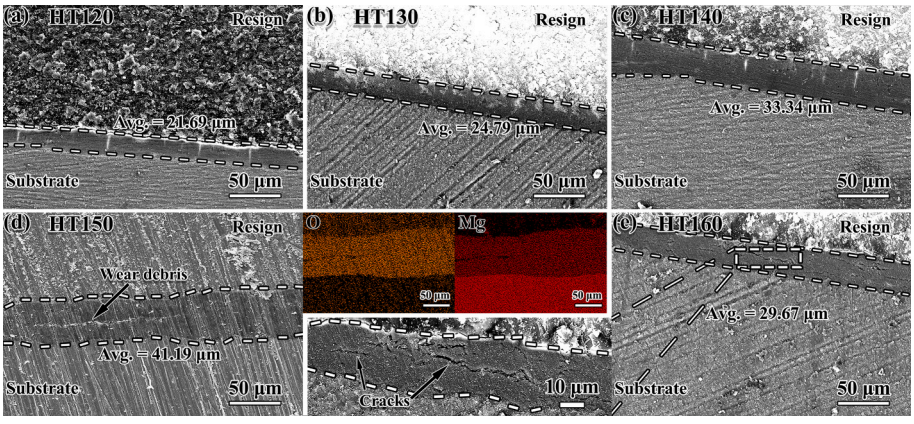

Fig. 6. Cross-sectional SEM morphologies of the MgAlCe-LDH/CeO_2 composite coating synthesized at (a) 120 °C, (b) 130 °C, (c) 140 °C, (d) 150 °C, and (e) 160 °C.

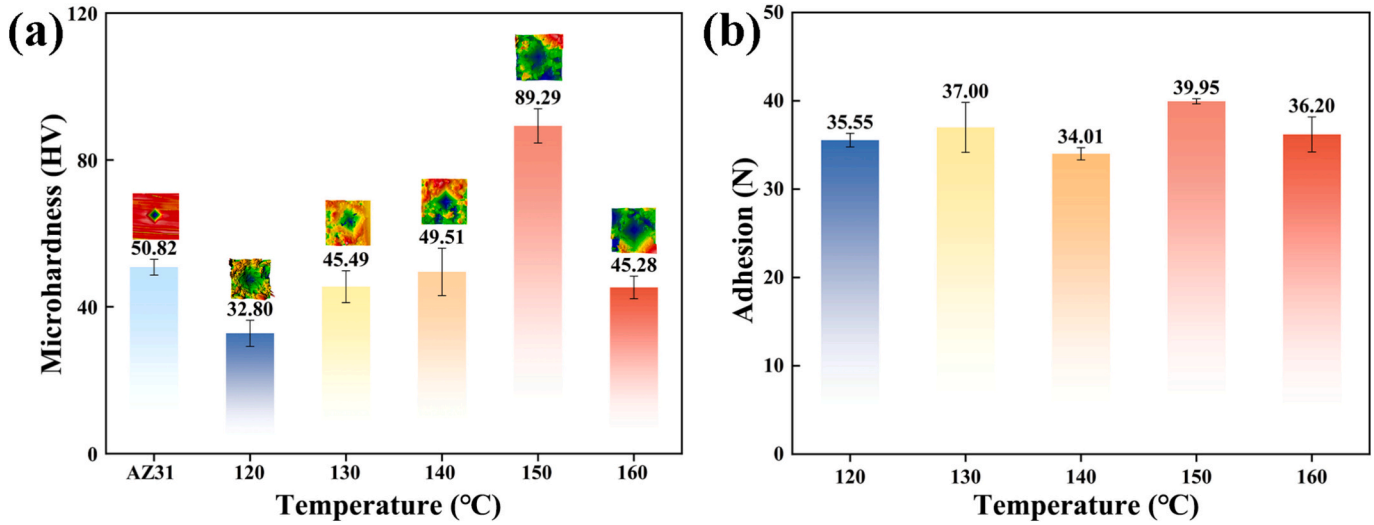

Fig. 7. Microhardness (a) and adhesion strength (b) of the MgAlCe-LDH/CeO_2 composite coating.

a maximum at 150 °C, before decreasing at higher temperatures. Within the range of 120 to 140 °C, the hardness gradually increased, but it did not exceed the hardness level of the AZ31 substrate. At 150 °C, hardness reached its maximum value (89.29 HV), showing a certain improvement compared to the substrate. At the same time, as shown in Fig. S3, it can also be seen that under the condition of a load of 300 gf, the hardness represented the combined effect of the coating and the substrate, which demonstrated the optimal hardness of the HT150 sample, and the overall trend was consistent. However, at 160 °C, the hardness decreased sharply. This evolution agrees with the previously discussed features in phase constitution and cross-sectional morphology. The HT150 sample exhibited the greatest thickness, best compactness, and an enriched presence of MgAlCe-LDH and CeO_2 phases, which together enhanced its load-bearing capacity. In contrast, coating at lower or excessively high temperatures exhibited microstructure aggregation and non-uniform deposition, compromising structure continuity and reducing hardness.

3.4.2. Adhesion strength

Fig. 7b shows the adhesion strength between the coating and the substrate. Although the overall variation was not as pronounced as that of microhardness, the temperature-dependent characteristics were still obvious. The coating prepared at 150 °C showed the strongest adhesion strength, while the coating prepared at 120–140 °C presented moderate strength. Due to structural degradation, the adhesion strength was slightly reduced at 160 °C. Cross-sectional analysis (Fig. 6) indicates that the HT160 sample exhibits substantial through-cracks. These defects serve as stress concentration locations and are the primary cause of adhesion strength reduction.

3.4.3. Coating stress

Residual stress was calculated by the Stoney Equation, as detailed in Section 6 in the Supplementary Material. The radius of curvature (R) after coating deposition increased from 4.35 m at 120 °C to 9.00 m at 150 °C as the hydrothermal temperature increased, indicating a continuous release of bending stress caused by the coating deposition process. Accordingly, the calculated residual stress decreased significantly from 0.56 GPa (HT120) to 0.04 GPa (HT140), resulting in a near-equilibrium stress state of 0.02 GPa at 150 °C. This trend demonstrated that as hydrothermal temperature increased, the coating thickened and its structure became denser, resulting in a progressive transition of the coating's stress state from tensile to a nearly equilibrated stress. As the hydrothermal temperature increased to 160 °C, the radius of curvature significantly decreased to 3.54 m, causing the residual stress to rise once again to 0.58 GPa. The phenomenon of increased stress may be attributed to the excessive crystallization, the presence of microstructural defects, and the stress accumulation resulting from the disparity in thermal expansion coefficients between the coating and the substrate under elevated temperatures. The results align with the surface morphological (Fig. 5) and the SEM observations of the coating cross-section (Fig. 6).

3.4.4. Fracture toughness

The fracture toughness (K_c) of coatings was quantitatively calculated by the Equation in Section 7 of the Supplementary Material. Akono et al. [33] proposed that the value of K_c reached a constant value when $d > d_{max}/2$, which was set as the fracture toughness of the coating. In this sense, the calculated fracture toughness values of HT120, HT130, HT140, HT150, and HT160 samples were 2.36, 2.89, 4.11, 13.23, and 5.34 MPa•$m^{1/2}$, respectively. Among them, the HT150 sample exhibited the largest fracture toughness. This performance was mainly attributed to its dense and defect-free microstructure, relatively high hardness, and excellent adhesion strength, which together inhibited crack propagation.

3.4.5. Surface roughness

The change law of surface roughness in Fig. 8 further confirms the trend of morphological changes. The surface of the HT150 sample showed dense and uniformly arranged nanosheets, resulting in the lowest roughness and the smoothest surface. The HT120 coating was slightly smoother than that of the substrate, but it did not reach the density achieved at 150 °C. Moreover, the coating prepared at 130 to 140 °C had higher roughness due to the irregular stacking of nanosheets, while the HT160 coating had the highest roughness due to particle aggregation and microstructural coarsening. These results were highly consistent with the SEM observations, indicating that an appropriate hydrothermal temperature was beneficial to the formation of continuous and uniformly oriented nanosheets, while excessively high temperatures degraded the layered structure of the coating.

3.5. Friction and wear performance

3.5.1. Coefficient of friction

As shown in Fig. 9a, the AZ31 substrate showed poor wear resistance, which is characterized by a high and fluctuating friction coefficient (0.24). This poor performance was due to the lack of protective surface coating. The COF value of the HT120 sample decreased at the beginning, but there were violent fluctuations and continuous instability after

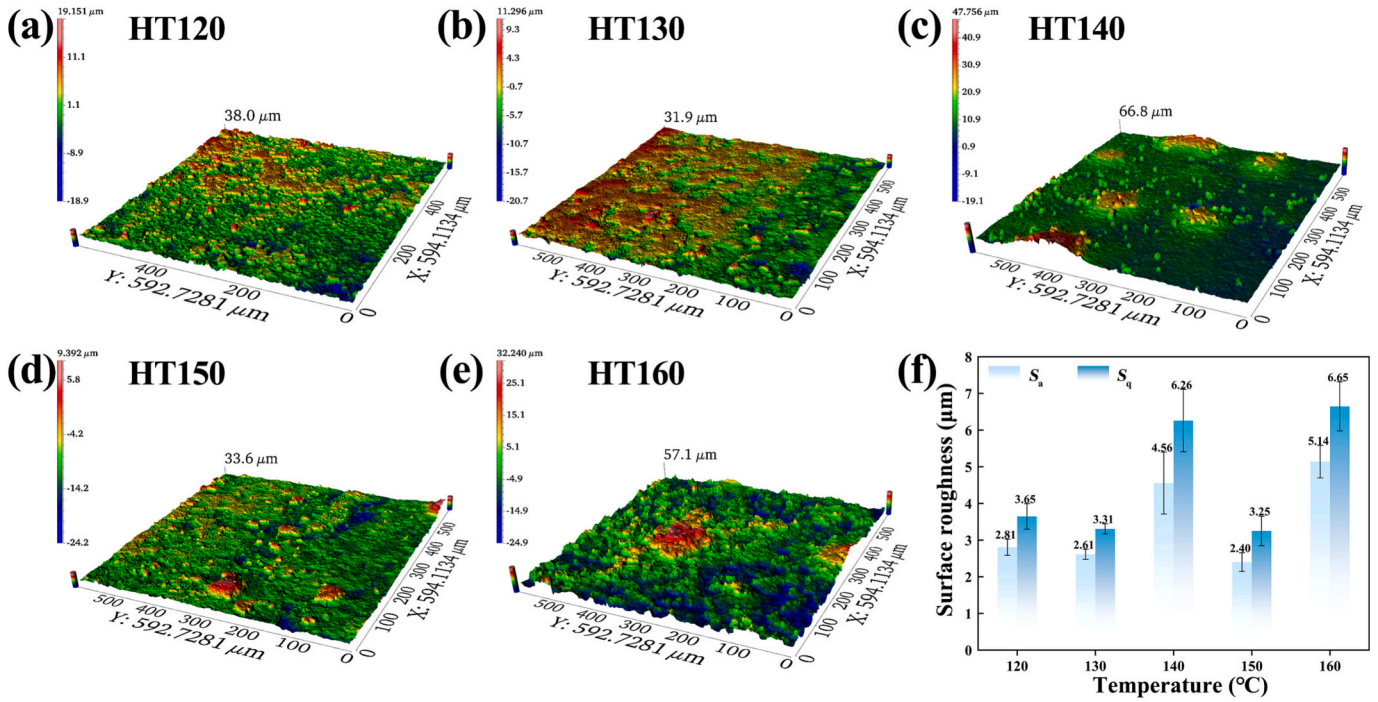

Fig. 8. Three-dimensional surface morphology of the MgAlCe-LDH/CeO_2 composite coating prepared at (a) 120 °C, (b) 130 °C, (c) 140 °C, (d) 150 °C, and (e) 160 °C, and the corresponding quantitative roughness parameters (f). S_a and S_q denote the average roughness and root-mean-square roughness, respectively.

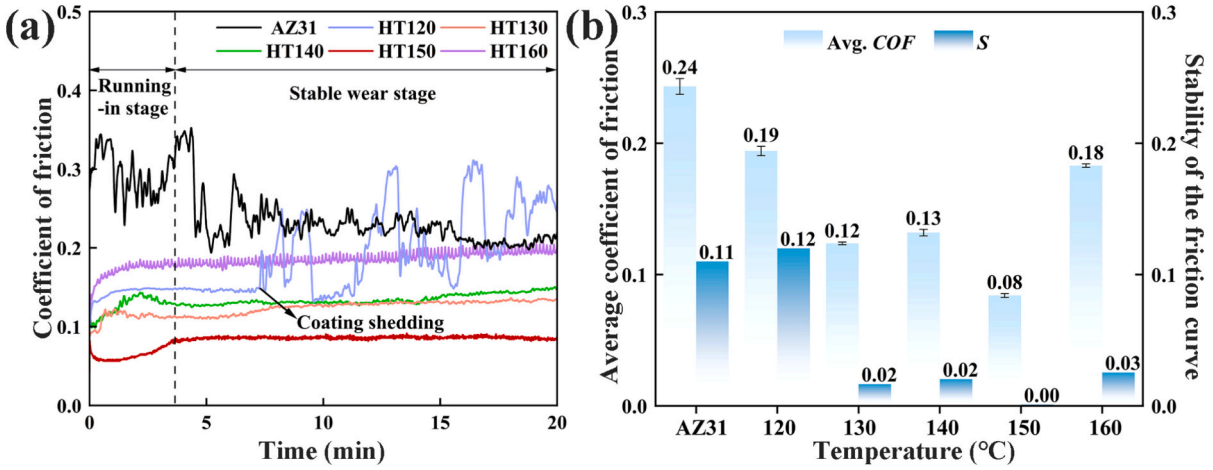

Fig. 9. Evolution of the friction coefficient with sliding time (a); average coefficient of friction (Avg. *COF*) and frictional stability analysis (b).

about 5 min, which was caused by the thin coating microstructure and more surface defects.

When the temperature was increased to 130 °C and 140 °C, the coating showed significantly better friction performance, starting from a lower COF and gradually stabilizing at 0.12 and 0.13, respectively. Under the current test conditions, the HT150 sample showed the best friction performance. Its COF started from a relatively low level, then experienced a slight decline, gradually rose, and finally reached a stable level. At steady-state conditions, the COF remained around 0.08 with little fluctuation (0.01). The good behavior observed at 150 °C was due to the optimization of coating thickness and compactness at this temperature, as well as the uniformity of the resulting microstructure. As for the HT160 sample, the average COF increased to 0.18, with a fluctuation of 0.03, reflecting the structural degradation caused by severe particle aggregation and crack formation at high temperature.

The test findings in Fig. 9a indicate that HT120 and HT160 samples exhibited poor tribological performances. Therefore, to further evaluate the long-term durability of these coatings, HT130, HT140, and HT150 samples were selected for long-term friction testing (Fig. 10a). The friction coefficients of HT130 and HT140 were stable in the early stage, but when the time exceeded 30 min, the friction curve fluctuated violently, indicating that the corresponding coatings began to peel off and fail. In contrast, the friction curve of the HT150 sample remained smooth after 120 min of long-term friction, and the coating had only slight surface wear. Under aggressive friction conditions (20 N, 10 Hz), the contact stress and friction temperature of the friction interface were significantly increased. Fig. 10c shows the rapid failure of HT130 and HT140 coatings, while the friction coefficient of the HT150 coating showed an upward trend until 8 min and then tended to stabilize. Although the HT150 coating eventually showed partial damage, it still showed significantly better peeling resistance and a relatively low friction coefficient than the rest of the samples under aggressive friction conditions, which fully demonstrated the excellent durability and long-term tribological reliability of the HT150 sample.

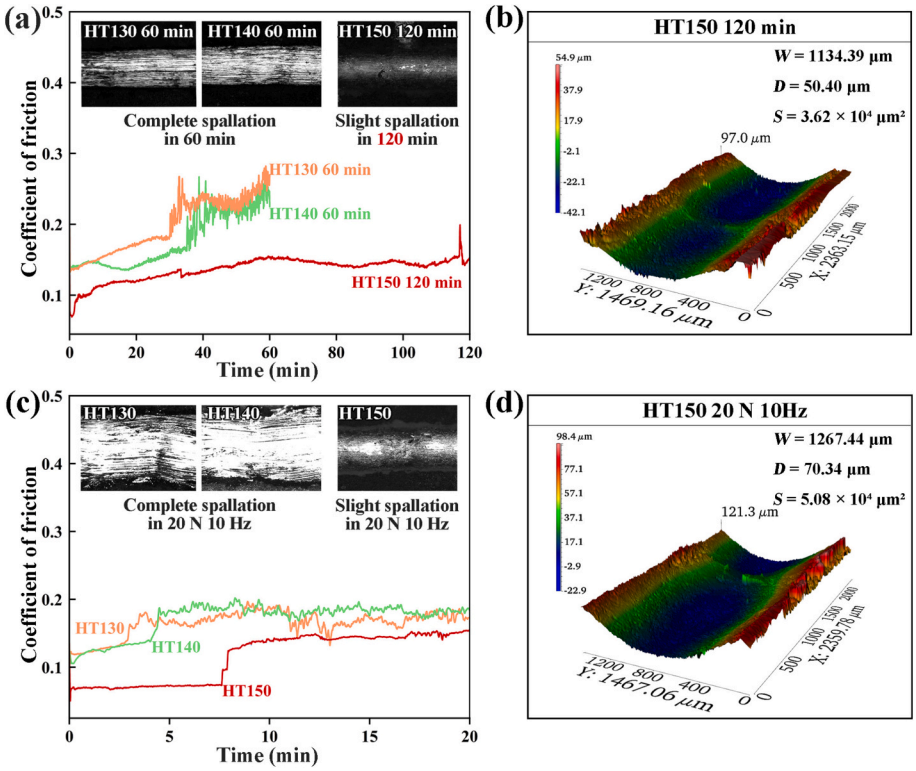

Fig. 10. Evolution of long-term friction coefficient with sliding time (a); 3D wear track profiles of HT150 sample after 120 min of sliding (b); Friction curve under the friction conditions of 20 N and 10 Hz (c); 3D wear track profiles of HT150 sample under the testing conditions of 20 N and 10 Hz (d).

3.5.2. Wear rate

Fig. 11 reveals the profile curve of the wear tracks, and Fig. 12 presents the wear rates calculated by Eq. (5). The AZ31 substrate experienced severe damage, showing deep and wide grooves, rough edges, and obvious tracks of plowing and tears. The wear mechanism was mainly controlled by adhesive wear and plastic deformation. The formation of the HT120 sample reduced the severity of overall wear; however, irregular depressions were still observed along the wear tracks. Limited by the thickness of the coating, there was a local layering phenomenon in the later stage of sliding. When the hydrothermal temperature increased to 130–140 °C, the wear groove became narrower and smoother, while the wear depth and wear rate decreased, which reflected the improvement of coating compactness and stronger interface adhesion.

Among all the samples, the HT150 coating was the most wear-resistant. Its wear trajectory appeared smooth and uniform, without obvious plowing or tearing, and the corresponding wear rate reached the lowest value of 0.39×10^{-4} $mm^3 \cdot N^{-1} \cdot m^{-1}$ (Fig. 12b). This finding was consistent with the lowest and most stable friction coefficients observed in Fig. 9. However, the wear-resistant properties of the HT160 coating decreased significantly. The wear trajectory deepened (Fig. 11f), and the wear rate increased significantly (Fig. 12b). This deterioration was caused by local stratification resulting from microstructural coarsening, crack propagation, and excessive reaction temperature, all of which damaged the integrity of the coating and reduced the wear stability. More importantly, Fig. 10b and d show that the wear rates of the HT150 coating under 120 min and aggressive friction conditions were 0.50×10^{-4} $mm^3 \cdot N^{-1} \cdot m^{-1}$ and 1.06×10^{-4} $mm^3 \cdot N^{-1} \cdot m^{-1}$, respectively, which were still lower than those of HT120, HT160, and the substrate. The combination of stable friction characteristics and a low long-term wear rate demonstrated the excellent durability and long-term frictional reliability of the HT150 sample.

3.5.3. Coating thickness and wear performance evaluation

Fig. 13a shows the comparison between the coating thickness obtained in this study and the values of the hydrothermal synthetic coatings prepared under different reaction times reported in the literature [16,31,34–44]. The coating produced here in just 3 h was significantly thicker than the representative example, which shows the efficiency of the manufacturing method. The production of a thicker coating in such a short reaction period reflected the optimized hydrothermal kinetics and provided a solid foundation for the observed superior friction properties. Fig. 13b compares the average COF and wear rates of samples prepared under different conditions, as well as the representative data from previous studies [24,44–55]. These comparisons are intended to be qualitative rather than quantitative, as there are differences in coating composition and testing conditions. The research results showed that the HT150 sample had a relatively low friction coefficient and wear rates. The research results showed that the HT150 sample had a low friction coefficient and wear rate, indicating that the MgAlCe-LDH/CeO_2 composite coating prepared in this study had excellent friction reduction and wear resistance over a short period. These results highlight the efficiency of the manufacturing process and its strong potential for practical application. The next section will provide a deep analysis of the intrinsic mechanism that leads to performance improvement.

4. Discussion

4.1. Formation and kinetic mechanism of MgAlCe-LDH/CeO_2 composite coating

As shown in the XRD (Fig. 3) and XPS (Fig. 4) spectra, the coating is mainly composed of $Mg(OH)_2$, CeO_2, and MgAlCe-LDH. SEM observations (Fig. 5) show a dense surface of uniformly oriented structures, indicating continuous in situ growth that sealed the surface defects. The whole reaction process was triggered by the local dissolution and interface alkalization of AZ31 Mg substrate, which were significantly

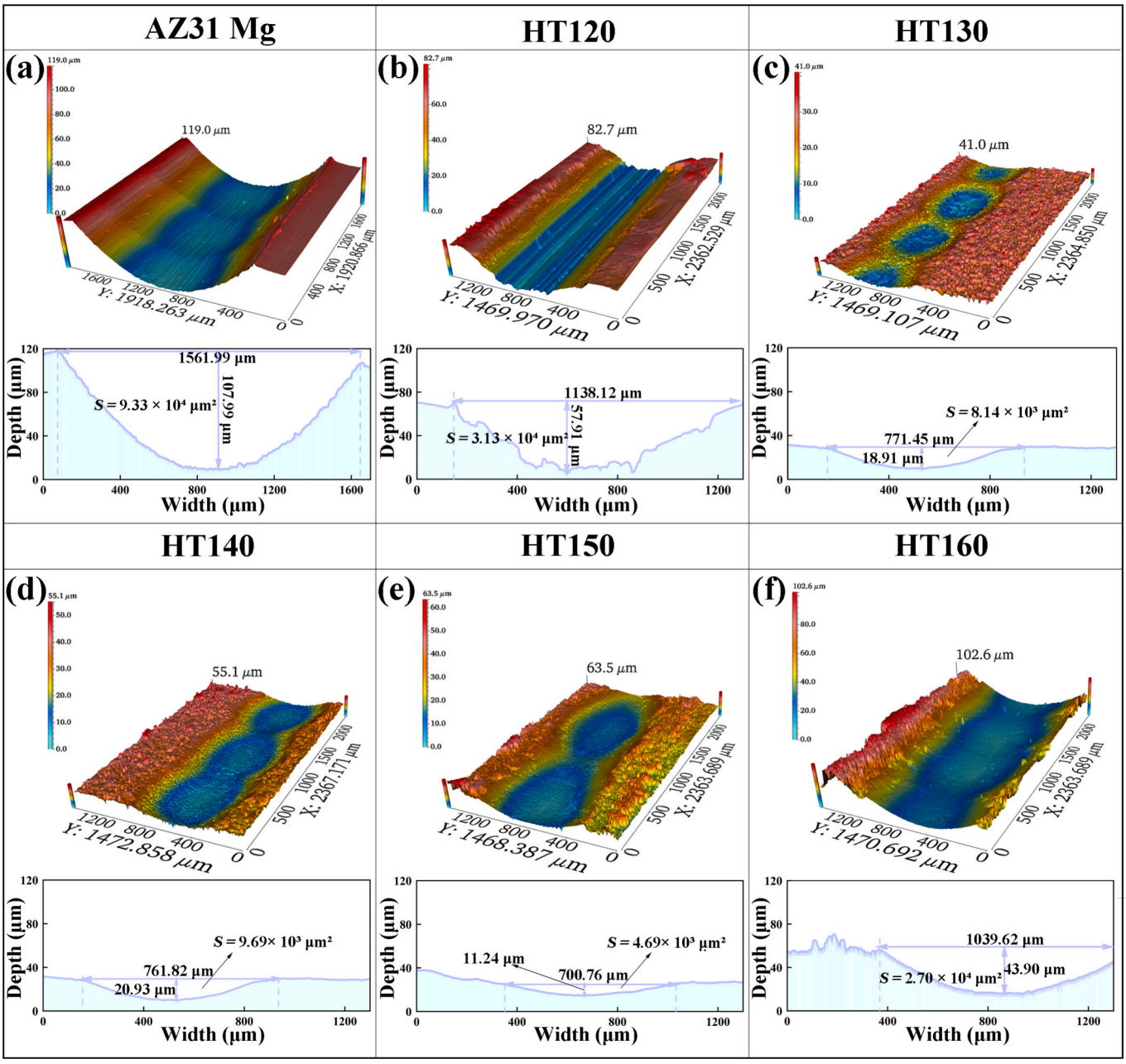

Fig. 11. Three-dimensional wear-track profiles of (a) the AZ31 Mg alloy and the MgAlCe-LDH/CeO_2 composite coating prepared at (b) 120 °C, (c) 130 °C, (d) 140 °C, (e) 150 °C, and (f) 160 °C.

affected by the hydrothermal temperature. The formation kinetics can be summarized as follows. At the initial stage, hydrogen evolution on the substrate produced $Mg(OH)_2$ (Eqs. (3)–(6)):

$$Mg \rightarrow Mg^{2+} + 2e^- \quad (3)$$

$$Al \rightarrow Al^{3+} + 3e^- \quad (4)$$

$$2H_2O + 2e^- \rightarrow 2OH^- + H_2\uparrow \quad (5)$$

$$Mg^{2+} + 2OH^- \rightarrow Mg(OH)_2\downarrow \quad (6)$$

As the local OH^- concentration increased, Al^{3+} species dissolved from the substrate and subsequently deposited (Eq. (7)). Simultaneously, the Ce^{3+} ions reacted with OH^- to form $Ce(OH)_3$ and $Ce(OH)_4$ precipitates (Eqs. (8)–(10)):

$$Al^{3+} + 3OH^- \rightarrow Al(OH)_3\downarrow \quad (7)$$

$$Ce^{3+} + 3OH^- \rightarrow Ce(OH)_3\downarrow \quad (8)$$

$$Ce^{3+} + 2OH^- \rightarrow Ce(OH)_2{}^{2+} + e^- \quad (9)$$

$$Ce(OH)_2{}^{2+} + 2OH^- \rightarrow Ce(OH)_4\downarrow \quad (10)$$

In an alkaline environment, NO_3^- anions, as interlayer species, maintained local charge neutrality, and promoted the transformation of $Mg(OH)_2$, $Al(OH)_4^-$, and $Ce(OH)_4^-$/$Ce(OH)_2{}^{2+}$ into the layered MgAlCe-LDH structure (Eqs. (11)–(13)):

$$(1-x)Mg^{2+} + xAl(OH)_4^- + NO_3^- + nH_2O \rightarrow Mg_{1-x}Al_x(OH)_{4x}(NO_3) \bullet nH_2O \quad (11)$$

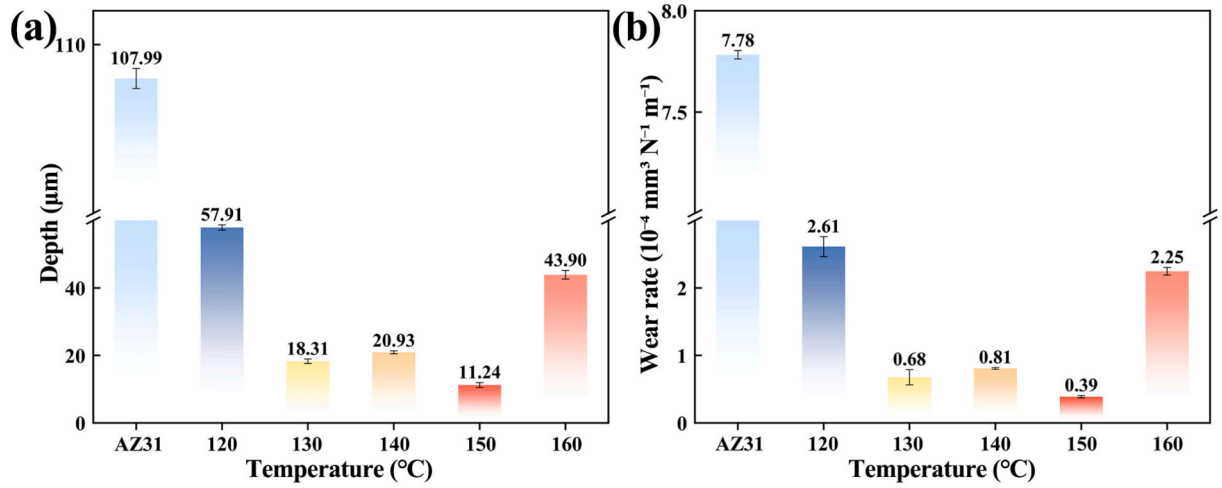

Fig. 12. (a) Wear depth and (b) wear rate of the AZ31 substrate and MgAlCe-LDH/CeO_2 composite coating.

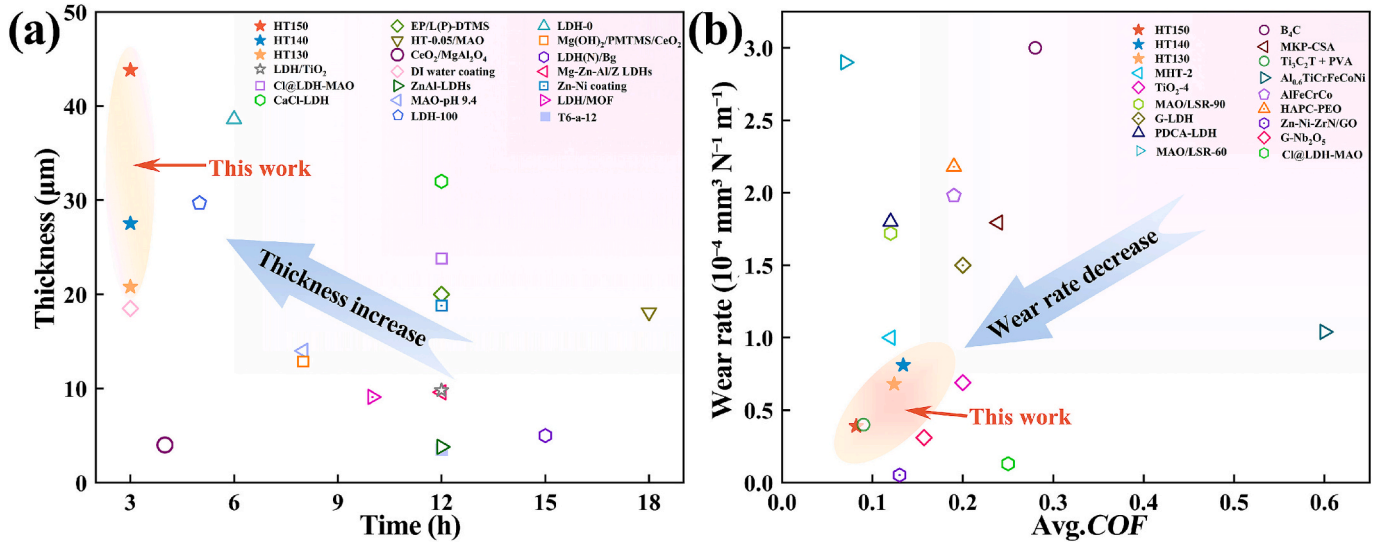

Fig. 13. Comparison of (a) coating thickness and (b) average coefficient of friction (Avg. *COF*) and wear rate for the MgAlCe-LDH/CeO_2 composite coating prepared at different hydrothermal temperatures.

$$(1-x)Mg^{2+} + xCe(OH)_4^- + NO_3^- + nH_2O \rightarrow Mg_{1-x}Ce_x(OH)_{4x}(NO_3) \bullet nH_2O \quad (12)$$

$$(1-x)Mg^{2+} + xCe(OH)_2^{2+} + 2NO_3^- + nH_2O \rightarrow Mg_{1-x}Ce_x(OH)_{2x}(NO_3)_2 \bullet nH_2O \quad (13)$$

Finally, some Ce hydroxide was dehydrated and oxidized to produce stable CeO_2 nanoparticles distributed within the LDH interlayers (Eqs. (14)–(15)):

$$Ce(OH)_3 \rightarrow CeO_2\downarrow + H_3O^+ + e^- \quad (14)$$

$$Ce(OH)_4 \rightarrow CeO_2\downarrow + 2H_2O \quad (15)$$

From a kinetic perspective, Ce ions accelerated the anodic dissolution of Mg and helped build a highly alkaline microenvironment. As the temperature rose, ion diffusion accelerated, so that the nucleation and growth processes reached a dynamic balance. A dense and thick coating was obtained at 150 °C. However, excessive temperature (160 °C) led to localized aggregation of the microstructure and reduced coating integrity, which was consistent with crystallization kinetics reported in continuous hydrothermal systems [56].

4.2. Thermodynamic mechanism of MgAlCe-LDH/CeO_2 composite coating

From a thermodynamic perspective, the incorporation of Ce^{3+}/Ce^{4+} modified the conventional nucleation behavior of MgAl-LDH and led to lattice distortion. Therefore, HTDI samples were prepared without the Ce element to separate the independent contributions of Ce and LDH, and a detailed analysis was provided in Section 5 of the Supplementary material. The XRD lattice parameter analysis (Table 2) indicates that the HT150 sample exhibits larger *d* values (8.13 Å for (003) and 4.06 Å for (006)) and *c*-axis parameters (average 24.375 Å) corresponding to about a 3.6% increment in the *c*-axis parameter compared with the HTDI

Table 2
The interplanar distance of LDH (003) and (006) planes in the composite coatings.

Sample	Diffraction peak	θ	*d* (Å)	*c* (Å)
HT150	(003)	10.91	8.13	24.39
	(006)	21.88	4.06	24.36
HTDI	(003)	11.31	7.84	23.52
	(006)	22.70	3.92	23.52

sample (d (003) = 7.84 Å, d (006) = 3.92 Å, c = 23.52 Å). This lattice distortion phenomenon was directly related to the redox behavior of Ce^{3+}/Ce^{4+}, confirmed by XPS analysis (Section 3.2.2). The XPS results show that Ce^{3+} and Ce^{4+} coexist in the coating, Ce^{4+} being the dominant valence state (CeO_2 as the main phase). The significant ionic radius difference between Ce^{3+} (1.143 Å) and Ce^{4+} (0.970 Å) causes lattice local strain during valence transition. When Ce ions entered the LDH interlayer or were distributed in the interlayer region, the abrupt change of ion radius broke the original lattice equilibrium and drove the expansion of interlayer spacing and c-axis size, which explained the quantitative change of lattice parameters of the HT150 sample.

In addition, the homogeneous lattice distortion induced by Ce redox, which is evidenced by the ideal layered relationship ($3 \times d$ (003) $\approx 6 \times d$ (006)) in the HT150 sample from XRD data (Table 2), confirms uniform lattice strain rather than local disorder. It produced a large number of lattice defects, such as dislocations and strain regions within the coating. These defects act as intrinsic active sites for heterogeneous nucleation, effectively lowering the critical nucleation energy barrier [57,58]. Unlike disordered dispersion at 120 °C or aggregation at 160 °C, the HT150 sample benefited from these uniformly distributed active sites, which promoted the uniformly oriented growth of MgAlCe-LDH and homogeneous dispersion of CeO_2 nanoparticles to form dense microstructures. In summary, the strong coordination ability of Ce^{3+}/Ce^{4+} contributes to the stability of the Ce-Mg-Al LDH system [59], causing lattice distortion and redox interactions, promoting coating densification and stabilizing the formation of the layer structure. The formation of CeO_2 nanoparticles not only filled the structural gaps but also improved the overall performance of the coating. As a key factor, hydrothermal temperature played a decisive role in the balance between nucleation kinetics, ion transport, and structural evolution and ultimately determined the quality of the coating. Fig. 16a shows the formation mechanism of MgAlCe-LDH/CeO_2 composite coating.

4.3. Hydrothermal temperatures on coating microstructure and mechanical response

Temperature played a decisive role in phase formation and nucleation-growth behavior. At lower temperatures (120 to 140 °C), the limited ion diffusion rate and low solvent activity suppressed the nucleation of the LDH phase and CeO_2 particles, resulting in sparse LDH nanosheets and a nonuniform Ce distribution within the coating. As shown in the weak LDH diffraction peak (Fig. 3) and the fractured porous surface morphology observed by SEM (Fig. 5), the structural integrity of the coating synthesized under low-temperature conditions was poor. When the temperature increased to 150 °C, the enhanced reactivity of the solution and accelerated ion migration promoted the uniformly oriented growth of the LDH lamellae and the homogeneous incorporation of Ce, thus forming a denser coating and a stronger synergy between the LDH and the CeO_2 phases. However, at 160 °C, the imbalance between nucleation and growth led to an increase in local aggregation, interface debonding and precipitation in the solution, which together damage the continuity of the coating.

The coating microstructure greatly influenced the resulting mechanical response. As illustrated in Fig. 6, the coating of the HT150 sample had the largest thickness (about 41.19 μm) with no visible cracks, exhibiting a dense and uniform microstructure. In contrast, the coating synthesized at 160 °C had wider and continuous through-thickness cracks, which seriously compromised the integrity of the interface. Tang et al. [60] also observed similar temperature-induced cracking in coatings containing LDH lamellae. Correspondingly, the HT150 sample demonstrated the largest microhardness (Fig. 7a), adhesion strength (Fig. 7b), fracture toughness (Fig. S6), and the least internal stress (0.02 GPa) with a near-equilibrium stress state, which was attributed to the uniform dispersion of CeO_2 nanoparticles within the dense and defect-free MgAlCe-LDH matrix. In contrast, the degraded mechanical properties of the HT160 counterpart were mainly attributed to the structural embrittlement and sharp decrease in fracture toughness caused by high temperature. Furthermore, excessive tensile residual stress due to severe dehydration shrinkage and thermal mismatch interacted with low toughness to induce wide and continuous through-thickness cracks (Fig. 6) that ultimately severely damaged the interfacial adhesion strength (Fig. 7).

In summary, the hydrothermal temperature influences the coating microstructure, which further impacts the coating's mechanical performance. Dense and crack-free coatings with uniformly distributed CeO_2 nanoparticles were formed at the ideal temperature of 150 °C. Microhardness, adhesion, and fracture toughness all increased synergistically with this ideal microstructure. Conversely, deviation from this optimal temperature (whether increased or decreased) will lead to microstructural defects, such as increased porosity, reduced cohesion, or cracking. Fig. 16b illustrates the effects of hydrothermal temperatures on coating microstructure and mechanical response.

4.4. Hydrothermal temperature on the wear mechanism of MgAlCe-LDH/CeO_2 composite coating

The wear surfaces of the HT120-HT140 samples (Fig. 14a-c) showed distinct plowing grooves and accumulated debris, suggesting that failure was mainly caused by the adhesive wear. This can be attributed to the limitation of the mechanical properties of the coatings, where the microhardness was insufficient to resist abrasive wear, and there was a high residual tensile stress. Furthermore, the low fracture toughness (2.36–4.11 $MPa \cdot m^{1/2}$) combined with the moderate adhesion strength could not inhibit the propagation of cracks under shear stress, thus aggravating the dominance of adhesive wear. This finding was consistent with the investigation on low-temperature MgAl-LDH coatings [61]. In addition, the HT160 sample exhibits irregular lamellar spalling and deep grooves (Fig. 14d), suggesting that the wear mechanism shifts to a mixed adhesive-fatigue wear. Although it was very thick, the structure was seriously degraded. The combination of excessive dehydration, microstructure agglomeration, and internal stress accumulation that developed at high hydrothermal temperatures resulted in cracks through the coating thickness and compromised the structural integrity [62]. Therefore, the coating cannot remain stable during friction (Fig. 9a). In contrast, the HT150 sample with densely interwoven MgAlCe-LDH lamellar and CeO_2 nanoparticles exhibited the best mechanical stability and long-term wear resistance (Fig. 10). The largest microhardness and maximum fracture toughness produced substantial resistance to plastic deformation and a significant reduction in residual stress levels (0.02 GPa). Coupled with its excellent adhesion strength and low surface roughness, it effectively reduced stress concentrations at the interface, thus preventing delamination of the coating during friction.

In order to gain a deeper understanding of the low friction performance of the HT150 coating, a detailed chemical composition analysis was carried out on the wear interface, and EDS surface analysis of the counterface balls and wear tracks was performed. The results showed that the Ce content in the wear marks was significantly reduced (Fig. 15a–a_1), whereas a transfer layer enriched in Mg, Al, O, and Ce was clearly detected on the counterface ball surface (Fig. 15b–b_1). Among them, the enrichment of Mg and Al indicated that LDH nanosheets were peeled off and attached to the ball surface under shear force, greatly facilitating interlayer sliding. The presence of Ce, on the other hand, likely stems from the release and subsequent transfer of CeO_2 nanoparticles from the coating matrix to the counterface surface along with wear debris during friction. The XPS spectra illustrations of Ce and O further support this explanation, confirming that Ce at the wear interface mainly exists in the form of Ce^{4+} (CeO_2). These findings were consistent with previous reports. For example, Zhang et al. [63] found that CeO_2 nanoparticles can participate in the construction of high-strength friction coatings as hard phases, thus significantly reducing the friction coefficient. Wei et al. [64] pointed out that CeO_2

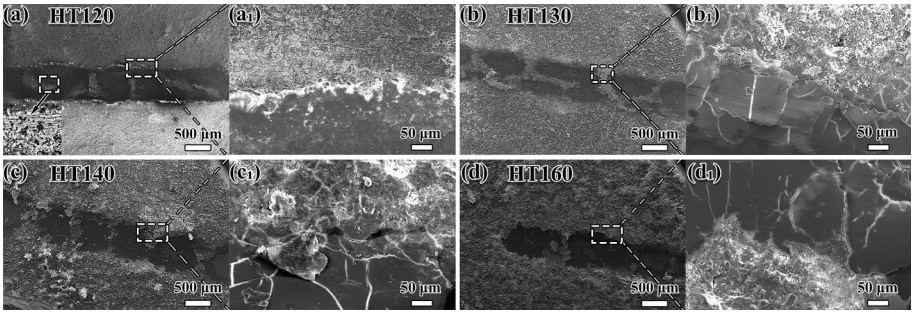

Fig. 14. SEM images of the worn surfaces of the MgAlCe-LDH/CeO_2 composite coating.

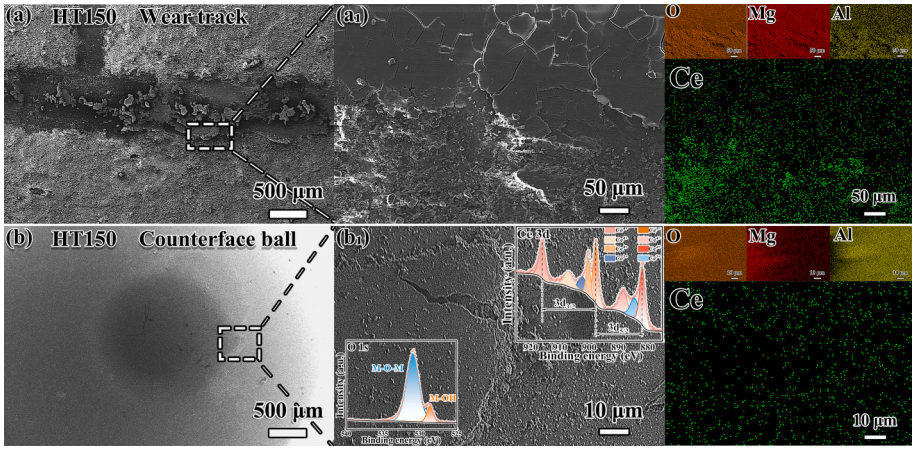

Fig. 15. SEM and the corresponding EDS scans of the wear-track edge (a-a_1) and transfer film on the counterface ball (b-b_1); The insets in (b_1) indicate XPS spectra for Ce and O of the transferred transfer film on the counterface ball.

nanoparticles provided a rolling effect and effectively improved the wear resistance of the coatings. Thus, in the HT150 coating, the improved mechanical properties ensured structural integrity and the combined effect of LDH interlayer shear and CeO_2 nanoparticle rolling lubrication promoted the formation of a self-lubricating transfer layer, which could partially isolate the friction contact surface and greatly reduce shear stress and coating wear rate, thereby achieving a long-term stable lubrication effect [65].

In summary, hydrothermal temperature controls the evolution of the wear resistance by regulating the density, microstructure and mechanical performance of the coating. At 150 °C, the sliding between the layers of LDH nanosheets and the load-bearing lubrication characteristics of CeO_2 nanoparticles act synergistically, forming a multi-scale wear resistance mechanism that includes interlayer sliding, dynamic transfer film formation and oxide coating-assisted self-repair. This comprehensive mechanism successfully reduced the shear stress at the interface, reduced material loss, and supported long-term friction stability. Fig. 16c shows that the hydrothermal temperature affects the wear mechanism of the MgAlCe-LDH/CeO_2 composite coating.

5. Conclusion

(1). The microstructure of the composite coating is hydrothermal temperature-dependent, which mainly consists of $Mg(OH)_2$, MgAlCe-LDH, and CeO_2 nanoparticles. At the optimum temperature of 150 °C, the introduction of Ce^{3+}/Ce^{4+} induced moderate lattice distortion and provided active nucleation sites. The resulting coating exhibits a dense, defect-free microstructure, preventing insufficient growth at lower temperatures or the agglomeration caused by higher temperatures.

(2). The HT150 coating achieves a synergistic balance of increased microhardness (89.29 HV) and excellent fracture toughness (13.23 $MPa{\cdot}m^{1/2}$). Characterized by a nearly neutral residual stress state (0.02 GPa) and superior resistance to plastic deformation, the coating efficiently suppresses crack initiation and brittle spalling under cyclic loading, demonstrating exceptional structural stability.

(3). A synergistic wear-resistant mechanism was identified, involving interlayer sliding of LDH and load-bearing/friction-reduction by CeO_2 nanoparticles. This multi-scale mechanism, which incorporates structural integrity, stress relaxation, and self-lubricating transfer film, allowed the HT150 coating to achieve a low stable friction coefficient (0.08) and wear rate (0.39×10^{-4} $mm^3{\cdot}N^{-1}{\cdot}m^{-1}$), thus avoiding severe adhesive wear.

(4). This study demonstrates the critical influence of hydrothermal temperature in improving the characteristics of MgAlCe-LDH/CeO_2 composite coating. The coating synthesized at 150 °C effectively attains optimal alignment between microstructural integrity and tribological properties. The results show that temperature-controlled hydrothermal synthesis is a feasible method for preparing high-performance Mg alloy protective coatings, which provides a feasible strategy for improving the service life of AZ31 Mg alloy in engineering applications.

CRediT authorship contribution statement

Feng Liu: Writing – original draft, Visualization, Validation, Investigation, Formal analysis, Data curation. **Peitao Guo:** Writing – review & editing, Validation, Methodology, Investigation, Formal analysis. **Zhen Li:** Investigation, Formal analysis, Data curation. **Lu Li:** Writing – review & editing, Validation, Supervision, Project administration,

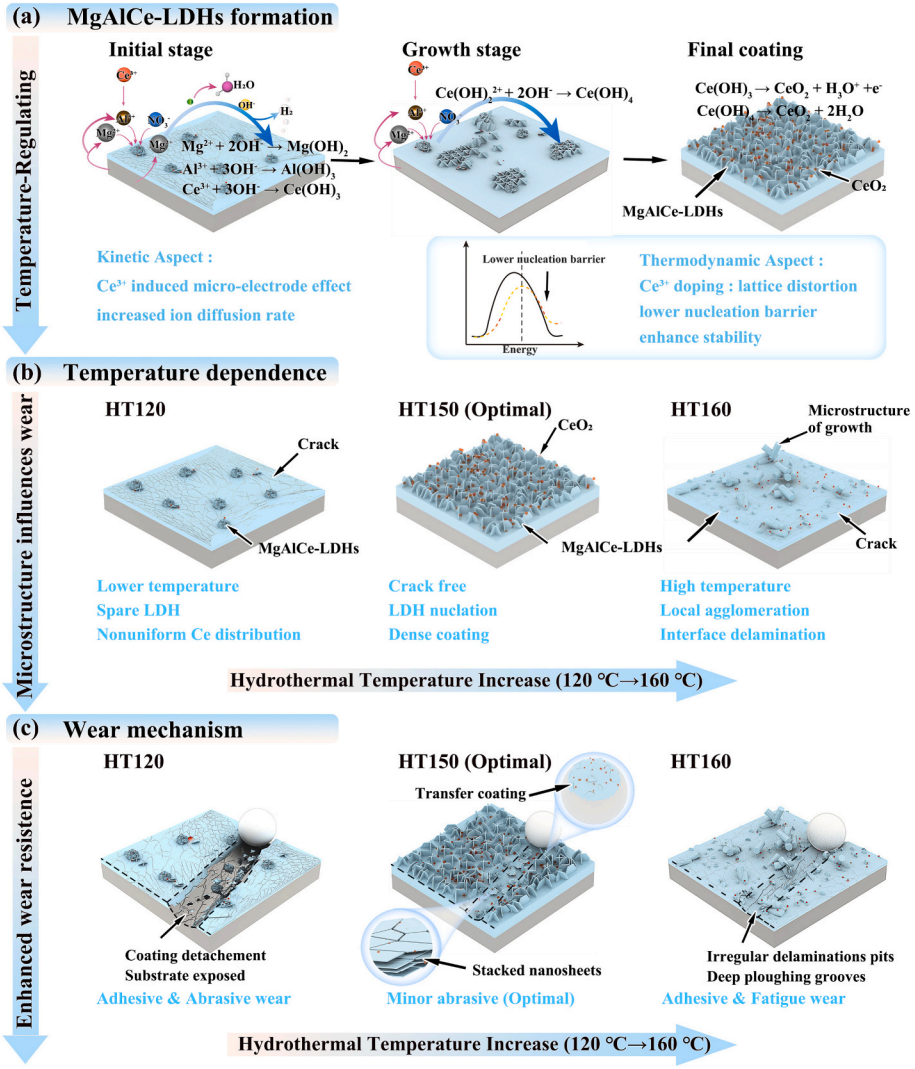

Fig. 16. Schematic illustration of (a) the formation mechanism of the MgAlCe-LDH/CeO_2 composite coating, (b) the effect of hydrothermal temperature on coating microstructure, and (c) the wear-resistance mechanism.

Methodology, Funding acquisition, Conceptualization.

Declaration of competing interest

The authors declare that they have no known competing financial interests or personal relationships that could have appeared to influence the work reported in this paper.

Acknowledgments

This work was financially supported by the Fundamental Research Funds for the Central Universities (SWU-KF25029), the Natural Science Foundation Project of CQ CSTC (CSTB2024NSCQ-MSX0473), and the Research Initiation Project under the Talent Introduction Program at Southwest University (SWU-KR24001). L. Li specially acknowledges Dr. Yifan Ruan at the Analytical & Testing Center of Southwest University for assistance in this study.

Appendix A. Supplementary data

Supplementary data to this article can be found online at https://doi.org/10.1016/j.surfcoat.2026.133329.

Data availability

Data will be made available on request.

References

[1] Y. Shao, R.-C. Zeng, S.-Q. Li, L.-Y. Cui, Y.-H. Zou, S.-K. Guan, et al., Advance in antibacterial magnesium alloys and surface coatings on magnesium alloys: a review, Acta Metall. Sin. (Engl. Lett.) 33 (2020) 615–629, https://doi.org/10.1007/s40195-020-01044-w.
[2] B. Liu, J. Yang, X. Zhang, Q. Yang, J. Zhang, X. Li, Development and application of magnesium alloy parts for automotive OEMs: a review, J. Magnesium Alloys 11 (2023) 15–47, https://doi.org/10.1016/j.jma.2022.12.015.
[3] Y. Liang, L. Li, Q. Zhou, Y. Ye, W. Jiang, Hot workability and microstructure development of Mg–8.0 Al–1.0 Yb–0.5 Zn magnesium alloy, J. Alloys Compd. 1047 (2025) 185029, https://doi.org/10.1016/j.jallcom.2025.185029.
[4] Y. Tian, S. Cao, W. Ma, F. Chen, S. Lu, Investigating microstructural characterization and tribological properties of AZ91D magnesium alloy reinforced with gradient nano-heterostructures through ultrasonic shot peening and laser melting process, Tribol. Int. 213 (2026) 111103, https://doi.org/10.1016/j.triboint.2025.111103.
[5] X. Bai, L. Li, Y. Xia, P. Xue, B. Zhang, Y. Duan, et al., Mechanical properties and in-vitro degradation behaviors of Mg–Yb extrusion alloys, J. Alloys Compd. 1039 (2025) 183158, https://doi.org/10.1016/j.jallcom.2025.183158.
[6] H. Duan, C. Yan, F. Wang, Effect of electrolyte additives on performance of plasma electrolytic oxidation films formed on magnesium alloy AZ91D, Electrochim. Acta 52 (2007) 3785–3793, https://doi.org/10.1016/j.electacta.2006.10.066.

[7] M. Campo, M. Carboneras, M.D. López, B. Torres, P. Rodrigo, E. Otero, et al., Corrosion resistance of thermally sprayed Al and Al/SiC coatings on Mg, Surf. Coat. Technol. 203 (2009) 3224–3230, https://doi.org/10.1016/j.surfcoat.2009.03.057.

[8] Y. Zhu, G. Wu, Y.-H. Zhang, Q. Zhao, Growth and characterization of $Mg(OH)_2$ film on magnesium alloy AZ31, Appl. Surf. Sci. 257 (2011) 6129–6137, https://doi.org/10.1016/j.apsusc.2011.02.017.

[9] J.H. Chu, G.X. Sun, L.B. Tong, Z.H. Jiang, Facile one-step hydrothermal fabrication of Allium giganteum-like superhydrophobic coating on Mg alloy with self-cleaning and anti-corrosion properties, Colloids Surf. A Physicochem. Eng. Asp. 617 (2021) 126370, https://doi.org/10.1016/j.colsurfa.2021.126370.

[10] S. Li, B. Bhushan, Lubrication performance and mechanisms of Mg/Al-, Zn/Al-, and Zn/Mg/Al-layered double hydroxide nanoparticles as lubricant additives, Appl. Surf. Sci. 378 (2016) 308–319, https://doi.org/10.1016/j.apsusc.2016.03.220.

[11] F. Peng, H. Li, D. Wang, P. Tian, Y. Tian, G. Yuan, et al., Enhanced corrosion resistance and biocompatibility of magnesium alloy by Mg–Al-layered double hydroxide, ACS Appl. Mater. Interfaces 8 (2016) 35033–35044, https://doi.org/10.1021/acsami.6b12974.

[12] S. Li, H. Qin, R. Zuo, Z. Bai, Tribological performance of Mg/Al/Ce layered double hydroxides nanoparticles and intercalated products as lubricant additives, Appl. Surf. Sci. 353 (2015) 643–650, https://doi.org/10.1016/j.apsusc.2015.05.091.

[13] S. Li, L. Ren, Z. Bai, Friction performance and mechanisms of calcined products of Mg/Al layered double hydroxides as lubricant additives, Appl. Surf. Sci. 470 (2019) 979–990, https://doi.org/10.1016/j.apsusc.2018.11.025.

[14] J. Zhang, D.-D. Lian, A.-R. Hou, Z.-H. Wang, M.-C. Zhang, J.W. Wu, et al., Comparative study on microstructure, corrosion morphology, and friction wear properties of layered double hydroxide/steam coating composite coatings on Mg–Li alloy, Adv. Eng. Mater. 26 (2024), https://doi.org/10.1002/adem.202400058.

[15] Y. Cao, D. Zheng, F. Zhang, J. Pan, C. Lin, Layered double hydroxide (LDH) for multi-functionalized corrosion protection of metals: a review, J. Mater. Sci. Technol. 102 (2022) 232–263, https://doi.org/10.1016/j.jmst.2021.05.078.

[16] J. Qin, Z. Zhang, W. Yao, L. Wu, L. Li, K. Wang, et al., LDH/MOF composite-layered slippery liquid-infused porous surface for excellent corrosion resistance and self-healing of AZ31 Mg alloy, Surf. Coat. Technol. (2025) 133061, https://doi.org/10.1016/j.surfcoat.2025.133061.

[17] C. Zhao, X. Wang, C. Li, Y. Liu, S. Sun, S. Yang, et al., Superior tribological and anti-corrosion performance of corrosion inhibitors intercalated LDH-MAO coating on AZ31 Mg alloys, Tribol. Int. 191 (2024) 109126, https://doi.org/10.1016/j.triboint.2023.109126.

[18] L. Wu, X. Ding, Z. Zheng, Y. Ma, A. Atrens, X. Chen, et al., Fabrication and characterization of an actively protective Mg-Al LDHs/Al_2O_3 composite coating on magnesium alloy AZ31, Appl. Surf. Sci. 487 (2019) 558–568, https://doi.org/10.1016/j.apsusc.2019.05.115.

[19] W. Yao, J. Qin, Y. Chen, L. Wu, B. Jiang, F. Pan, SiO_2 nanoparticles-containing slippery-liquid infused porous surface for corrosion and wear resistance of AZ31 Mg alloy, Mater. Des. 227 (2023) 111721, https://doi.org/10.1016/j.matdes.2023.111721.

[20] G. Jena, R. Chellappandian, L. Neelakantan, I. Adlakha, Development of potentiostatically deposited cerium conversion coating for Mg alloys, Mater. Corros. 75 (2024) 1313–1330, https://doi.org/10.1002/maco.202414420.

[21] H.R. Chauhan, S. Saladi, S. Variya, A. Solanki, S. Tailor, K.P. Sooraj, et al., Role of micro- and nano-CeO_2 reinforcements on characteristics and tribological performance of HVOF sprayed Cr_3C_2-NiCr coatings, Surf. Coat. Technol. 467 (2023) 129684, https://doi.org/10.1016/j.surfcoat.2023.129684.

[22] S. Yasmeen, M.R. Khan, K. Park, Y. Cho, J.W. Choi, H.-S. Moon, et al., Preparation of a hydrophobic cerium oxide nanoparticle coating with polymer binder via a facile solution route, Ceram. Int. 46 (2020) 12209–12215, https://doi.org/10.1016/j.ceramint.2020.01.268.

[23] S. Nayak, K.M. Parida, Nanostructured CeO_2/MgAl-LDH composite for visible light induced water reduction reaction, Int. J. Hydrog. Energy 41 (2016) 21166–21180, https://doi.org/10.1016/j.ijhydene.2016.08.062.

[24] L. Ren, S. Gao, Z. Chen, D. Jiang, H. Huang, Facile preparation of wear-resistant and anti-corrosion films on magnesium alloy, Surf. Eng. 38 (2022) 22–29, https://doi.org/10.1080/02670844.2021.2025312.

[25] L. Wu, F. Pan, Y. Liu, G. Zhang, A. Tang, A. Atrens, Influence of pH on the growth behaviour of Mg–Al LDH films, Surf. Eng. 34 (2018) 674–681, https://doi.org/10.1080/02670844.2017.1382062.

[26] A.P.B. dos Santos, T.C.M. Dantas, J.A.P. Costa, L.D. Souza, J.M. Soares, V.P. S. Caldeira, et al., Formation of CeO_2 nanotubes through different conditions of hydrothermal synthesis, Surf. Interfaces 21 (2020) 100746, https://doi.org/10.1016/j.surfin.2020.100746.

[27] G. Zhang, L. Wu, A. Tang, X.-B. Chen, Y. Ma, Y. Long, et al., Growth behavior of MgAl-layered double hydroxide films by conversion of anodic films on magnesium alloy AZ31 and their corrosion protection, Appl. Surf. Sci. 456 (2018) 419–429, https://doi.org/10.1016/j.apsusc.2018.06.085.

[28] J. Yang, K. Dong, Y. Song, A. Butt, Y. Cai, X. Cheng, et al., Study on self-healing electrophoretic composite coatings on magnesium alloys: modification mechanism of cerate and its influence, Surf. Coat. Technol. 510 (2025) 132231, https://doi.org/10.1016/j.surfcoat.2025.132231.

[29] X. Yu, G. Li, XPS study of cerium conversion coating on the anodized 2024 aluminum alloy, J. Alloys Compd. 364 (2004) 193–198, https://doi.org/10.1016/s0925-8388(03)00502-4.

[30] F. Zhang, Z.-G. Liu, R.-C. Zeng, S.-Q. Li, H.-Z. Cui, L. Song, et al., Corrosion resistance of Mg–Al-LDH coating on magnesium alloy AZ31, Surf. Coat. Technol. 258 (2014) 1152–1158, https://doi.org/10.1016/j.surfcoat.2014.07.017.

[31] L. Guo, F. Zhang, L. Song, R.-C. Zeng, S.-Q. Li, E.-H. Han, Corrosion resistance of ceria/polymethyltrimethoxysilane modified magnesium hydroxide coating on AZ31 magnesium alloy, Surf. Coat. Technol. 328 (2017) 121–133, https://doi.org/10.1016/j.surfcoat.2017.08.039.

[32] Y. Lin, S. Cai, S. Jiang, D. Xie, R. Ling, J. Sun, et al., Enhanced corrosion resistance and bonding strength of Mg substituted β-tricalcium phosphate/$Mg(OH)_2$ composite coating on magnesium alloys via one-step hydrothermal method, J. Mech. Behav. Biomed. Mater. 90 (2019) 547–555, https://doi.org/10.1016/j.jmbbm.2018.11.007.

[33] A.-T. Akono, F.-J. Ulm, An improved technique for characterizing the fracture toughness via scratch test experiments, Wear 313 (2014) 117–124, https://doi.org/10.1016/j.wear.2014.02.015.

[34] C. Zhao, X. Wang, C. Li, Y. Liu, S. Sun, S. Yang, et al., Superior tribological and anti-corrosion performance of corrosion inhibitors intercalated LDH-MAO coating on AZ31 Mg alloys, Tribol. Int. 191 (2024) 109126, https://doi.org/10.1016/j.triboint.2023.109126.

[35] G. Peng, Q. Qiao, L. Jin, B. Zhang, Y. Wang, K. Huang, et al., A novel CeO_2/$MgAl_2O_4$ composite coating for the protection of AZ31 magnesium alloys, J. Mater. Sci. 55 (2019) 1727–1737, https://doi.org/10.1007/s10853-019-03992-w.

[36] Z. Wang, J. Zhang, L. Bai, G. Zhang, Effects of Al^{3+} concentration in hydrothermal solution on the microstructural and corrosion resistance properties of fabricated MgO ceramic layer on AZ31 magnesium alloy, Mater. Corros. 72 (2020) 620–632, https://doi.org/10.1002/maco.202011948.

[37] Y. Zhu, Q. Zhao, Y.-H. Zhang, G. Wu, Hydrothermal synthesis of protective coating on magnesium alloy using de-ionized water, Surf. Coat. Technol. 206 (2012) 2961–2966, https://doi.org/10.1016/j.surfcoat.2011.12.029.

[38] Y. Wang, N. Huang, Y. Zhang, L. Liu, X. Zhao, Y. Yang, et al., Construction of superhydrophobic composite coating on AZ31B Mg alloy for improved corrosion resistance and anti-wear property, J. Alloys Compd. 1005 (2024) 176039, https://doi.org/10.1016/j.jallcom.2024.176039.

[39] X. Wang, L. Yan, K. Gao, P. Li, J. Hao, Enhancing the corrosion resistance of ZnAl-LDHs films on AZ91D magnesium alloys by designing surface roughness, Coatings 13 (2023) 724, https://doi.org/10.3390/coatings13040724.

[40] Z. Yao, Q. Xia, L. Chang, C. Li, Z. Jiang, Structure and properties of compound coatings on Mg alloys by micro-arc oxidation/hydrothermal treatment, J. Alloys Compd. 633 (2015) 435–442, https://doi.org/10.1016/j.jallcom.2015.02.008.

[41] Z. Dou, Y. Zhang, T. Shulha, R. Cui, M. Serdechnova, H. Tian, et al., Insight into chelating agent stimulated in-situ growth of MgAl-LDH films on magnesium alloy AZ31: the effect of initial cationic concentrations, Surf. Coat. Technol. 439 (2022) 128414, https://doi.org/10.1016/j.surfcoat.2022.128414.

[42] J. Ouyang, X. Hong, Y. Gao, Retardation and self-repair of erosion pits by a two-stage barrier on bioactive-glass/layered double hydroxide coating of biomedical magnesium alloys, Surf. Coat. Technol. 405 (2021) 126562, https://doi.org/10.1016/j.surfcoat.2020.126562.

[43] Y. Chen, L. Wu, W. Yao, J. Wu, Z. Xie, Y. Yuan, et al., In situ growth of Mg-Zn-Al LDHs by ZIF-8 carrying Zn source and micro-arc oxidation integrated coating for corrosion and protection of magnesium alloys, Surf. Coat. Technol. 451 (2022) 129032, https://doi.org/10.1016/j.surfcoat.2022.129032.

[44] H. Wang, L. Zhang, Y. Li, Y. Huang, J. Guo, S. Li, et al., ZrN/GO nanocomposite synergistic optimization of friction and corrosion behavior of Zn Ni coatings, Surf. Coat. Technol. 519 (2026) 132944, https://doi.org/10.1016/j.surfcoat.2025.132944.

[45] G. Yang, K. Yang, J. Yang, J. Chen, W. Li, Z. Zhang, et al., Wear and corrosion resistance of AZ31B magnesium alloy micro-arc oxide coatings by laser surface remelting, Vacuum 240 (2025) 114435, https://doi.org/10.1016/j.vacuum.2025.114435.

[46] K. Zhang, W. Zhang, Y. Yang, X. Sun, B. Men, S. Yu, Enhanced hydrophobic properties, wear and corrosion resistance of plasma electrolyte oxidation coatings on AZ31B magnesium alloys with addition of TiO_2 nanoparticles, Ceram. Int. 50 (2024) 52941–52956, https://doi.org/10.1016/j.ceramint.2024.10.145.

[47] H. Wu, Y. Zhang, S. Long, L. Zhang, X. Jie, Tribological behavior of graphene anchored Mg-Al layered double hydroxide film on Mg alloy pre-sprayed Al coating, Appl. Surf. Sci. 530 (2020) 146536, https://doi.org/10.1016/j.apsusc.2020.146536.

[48] Y. Wu, L. Wu, L. Wang, C. Wang, F. Yu, W. Yao, et al., Electrophoretic deposition of MXene coating on Mg alloy 2,5 PDCA-LDH film for enhanced anticorrosion/wear, Colloids Surf. A Physicochem. Eng. Asp. 702 (2024) 135043, https://doi.org/10.1016/j.colsurfa.2024.135043.

[49] V. Titarmare, S. Banerjee, P. Sahoo, Abrasive wear behavior of AZ31 −B_4C composites, Tribol. Int. 194 (2024) 109455, https://doi.org/10.1016/j.triboint.2024.109455.

[50] X. Li, R. Ke, E. Lin, J. Liu, D. Chen, S.-Z. Kure-Chu, et al., Multifunctional MOF-based composite coating on Mg alloy for biodegradable orthopedic implants, Appl. Surf. Sci. 692 (2025) 162727, https://doi.org/10.1016/j.apsusc.2025.162727.

[51] Y. Wang, H. Bao, A. Tang, X. Lu, N. Yuan, J. Ding, $Ti_3C_2T_x$-based composite coating on AZ31B Mg alloy surface for improved anti-corrosion/wear-reducing properties, Mater. Today Commun. 35 (2023) 105664, https://doi.org/10.1016/j.mtcomm.2023.105664.

[52] L. Chen, K. Bobzin, Z. Zhou, L. Zhao, M. Öte, T. Königstein, et al., Wear behavior of HVOF-sprayed Al0.6TiCrFeCoNi high entropy alloy coatings at different temperatures, Surf. Coat. Technol. 358 (2019) 215–222, https://doi.org/10.1016/j.surfcoat.2018.11.052.

[53] D. Zhao, T. Yamaguchi, D. Tusbasa, W. Wang, Fabrication and friction properties of the AlFeCrCo medium-entropy alloy coatings on magnesium alloy, Mater. Des. 193 (2020) 108872, https://doi.org/10.1016/j.matdes.2020.108872.

[54] T. Xie, C. Jiang, B. Ning, W. Qian, L. Shi, Y. Chen, Wear-resistant enhanced composite coatings on TC_4: combining halide-activated pack cementation and plasma electrolytic oxidation, Surf. Coat. Technol. 489 (2024) 131161, https://doi.org/10.1016/j.surfcoat.2024.131161.
[55] Z. Ding, Q. Yuan, H. Wang, Y. Tang, Y. Tan, Q. He, Microstructure and properties of Nb_2O_5/Mg gradient coating on AZ31 magnesium alloy by magnetron sputtering, Ceram. Int. 49 (2023) 154–167, https://doi.org/10.1016/j.ceramint.2022.08.324.
[56] I. Clark, P.W. Dunne, R.L. Gomes, E. Lester, Continuous hydrothermal synthesis of Ca_2Al-NO_3 layered double hydroxides: the impact of reactor temperature, pressure and NaOH concentration on crystal characteristics, J. Colloid Interface Sci. 504 (2017) 492–499, https://doi.org/10.1016/j.jcis.2017.05.105.
[57] Ce-induced synergistic effect in exsolved perovskite catalyst for highly efficient and robust methane dry reforming | Nat. Commun. n.d. https://www.nature.com/articles/s41467-025-65619-w (accessed January 24, 2026).
[58] D. Ma, Z. Lu, Y. Tang, T. Li, Z. Tang, Z. Yang, Effect of lattice strain on the oxygen vacancy formation and hydrogen adsorption at CeO_2(111) surface, Phys. Lett. A 378 (2014) 2570–2575, https://doi.org/10.1016/j.physleta.2014.07.006.
[59] D.E.L. Vieira, A.N. Salak, M.G.S. Ferreira, J.M. Vieira, C.M.A. Brett, Ce-substituted Mg-Al layered double hydroxides to prolong the corrosion protection lifetime of aluminium alloys, Appl. Surf. Sci. 573 (2022) 151527, https://doi.org/10.1016/j.apsusc.2021.151527.
[60] L. Tang, X. Jiang, Q. Zheng, D. Lin, Hydrothermal temperature-driven evolution of morphology and electrocatalytic properties of hierarchical nanostructured CoFe-LDHs as highly efficient electrocatalysts for oxygen evolution reactions, Dalton Trans. 51 (2022) 211–219, https://doi.org/10.1039/d1dt03101e.
[61] C. Wang, B. Liu, P. Wei, K. Xie, Y. Chen, M. Wang, et al., Optimization of Mg–Al layered double hydroxide film preparation and corrosion resistance study on AZ91D Mg alloy by multivariate polynomial regression fitting, ACS Omega 9 (2024) 19158–19168, https://doi.org/10.1021/acsomega.3c10297.
[62] El-Monaem EMA, H.M. Elshishini, S.S. Bakr, H.G. El-Aqapa, M. Hosny, G. Andaluri, et al., A comprehensive review on LDH-based catalysts to activate persulfates for the degradation of organic pollutants, NPJ Clean Water 6 (2023), https://doi.org/10.1038/s41545-023-00245-x.
[63] C. Shi, H. Zhang, J. Jia, X. Xing, T. Li, Y. Zhang, et al., Synergistic lubrication mechanism of CeO_2 nano-additives and friction modifiers in PAO/DLC solid-liquid composite lubricating system, Tribol. Int. 204 (2025) 110499, https://doi.org/10.1016/j.triboint.2024.110499.
[64] X. Wei, W. Chen, C. Wang, T. Feng, Y. Fu, Utilizing CeO_2 modified graphene for enhancing tribological performance of lubricating oils, Surf. Interfaces 72 (2025) 107078, https://doi.org/10.1016/j.surfin.2025.107078.
[65] Q.Y. Mao, X. Zhang, Z. Yu, S. Shi, Z. Liu, Y. Zhao, Multi-Layer Structure Improves Wear and Corrosion Resistance of Chromium, 2025, https://doi.org/10.2139/ssrn.5182559.